

Nano-sized BaSnO₃ powder via a precursor route: Comparative study of sintering behaviour and mechanism of fine and coarse-grained powders

Roberto Köferstein*, Lothar Jäger, Mandy Zenkner, Stefan G. Ebbinghaus

Institut für Chemie/Anorganische Chemie, Martin-Luther-Universität Halle-Wittenberg, Kurt-Mothes Strasse 2, D-06120 Halle, Germany

Received 21 November 2008; received in revised form 19 January 2009; accepted 22 January 2009

Available online 23 February 2009

Abstract

Preparation of a very fine BaSnO₃ powder by calcination of a barium tin 1,2-ethanediolato complex precursor and its sintering behaviour are described herein. A rate controlled calcination process to 820 °C leads to a nm-sized BaSnO₃ powder with a specific surface area of $S = 15.1 \text{ m}^2/\text{g}$ ($d_{\text{av}} = 55 \text{ nm}$). The powder has a slightly larger cell parameter of $a = 412.22(7) \text{ pm}$ compared to the single crystal value, which decreases with increasing calcination temperature and reaches the reference value above 1000 °C. The sintering behaviour is compared between fine and coarse-grained BaSnO₃ powders. Corresponding powder compacts of the nano-sized BaSnO₃ achieve a relative density of 90% after sintering at 1600 °C for 1 h and at 1500 °C and a soaking time of 30 h, whereas coarse-grained powder compacts reach only 80% of the relative density at 1650 °C (10 h). Furthermore, the shrinkage mechanisms of fine and coarse-grained powder compacts have been investigated and are discussed. © 2009 Elsevier Ltd. All rights reserved.

Keywords: Sintering; Perovskites; Precursors-organic; Grain size; Ceramics

1. Introduction

Barium stannate and its solid solutions (e.g. BaTi_{1-x}Sn_xO₃) have found important applications in materials science and technology due to their dielectric properties.^{1–5} Pure and doped barium stannate can be used as material for semiconductor gas sensors. It has been reported that sensors based on BaSnO₃ are sensitive to a variety of gases, e.g. CO, O₂, C₂H₅OH, CH₃SH, LPG and NO_x.^{6–12} Additionally, the results by Borse et al.^{13,14} and Yuan et al.¹⁵ suggest that BaSnO₃-based systems could be candidates for photocatalytic applications. Mizoguchi et al.¹⁶ reported that BaSnO₃ exhibits strong near-infrared luminescence at room temperature.

The conventional mixed-oxide method requires high temperatures and results in coarse-grained powders.^{17,18} Compacts of those powders show moderate densification behaviours. In the last years many preparation procedures have been published to obtain fine-grained BaSnO₃ powders at relatively low temperatures. Different hydrothermal methods or sol–gel processes

have been developed.^{19–23} A peroxide method was reported by Pfaff²⁴ to synthesise phase pure BaSnO₃. Recently, a lyothermal synthesis at 250 °C has been reported by Lu and Schmidt.²⁵ Various precursor complexes, coprecipitation and polymerised complex methods have also been developed to obtain barium stannate powders.^{26–29} Based on the exothermic reaction of suitable solids, self-propagating high temperature syntheses (SHS; also described as self-heat-sustained synthesis) are also used to prepare BaSnO₃.^{30,31}

In our previous works,^{29,32} we have reported on the preparation and structure of a precursor complex – [Ba(HOC₂H₄OH)₄][Sn(OC₂H₄O)₃]—and its conversion into BaSnO₃. This precursor is suitable to form solid solutions of the type [Ba(HOC₂H₄OH)₄][Ti_{1-x}Sn_x(OC₂H₄O)₃], which can be decomposed to phase pure fine-grained BaTi_{1-x}Sn_xO₃ powders.³³

This publication reports on the preparation of a nm-sized BaSnO₃ powder, prepared by the decomposition of a barium tin 1,2-ethanediolato complex precursor, the sintering behaviour and mechanism of resulting powder compacts. For comparative purposes, coarse-grained BaSnO₃ powders (mixed-oxide method) have also been studied.

* Corresponding author. Tel.: +49 345 5525630; fax: +49 345 5527028.
E-mail address: roberto.koefersteinst@chemie.uni-halle.de (R. Köferstein).

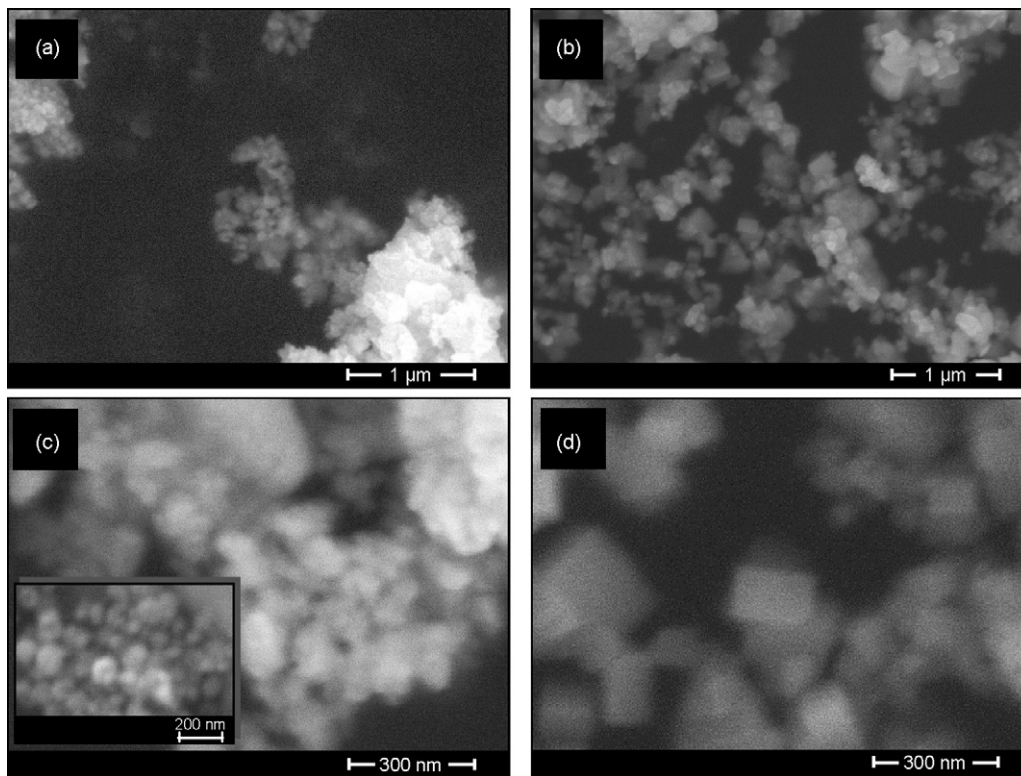


Fig. 1. SEM images of powders **1a** (a, b) and **2** (c, d) with different magnifications.

2. Experimental

2.1. Material preparation

The preparation procedure for $[\text{Ba}(\text{HOC}_2\text{H}_4\text{OH})_4][\text{Sn}(\text{OC}_2\text{H}_4\text{O})_3]$ (**1**) has been described elsewhere.^{29,32} For a better reproducibility we modified that procedure. SnCl_4 (0.10 mol; Laborchemie Apolda) was slowly added to ice-cold water (800 mL), and then a concentrated ammonia solution was added to adjust a pH value of 7–7.5. The precipitate was slowly filtered off and washed with water until the filtrate was almost free from Cl^- ions. A suspension of this wet precipitate ($\text{SnO}_2 \cdot n\text{H}_2\text{O}$) with $\text{Ba}(\text{OH})_2 \cdot 8\text{H}_2\text{O}$ (0.10 mol; Fluka) and 800 mL 1,2-ethanediol was stirred overnight at room temperature in argon atmosphere. Thereafter the suspension was heated to remove water. Afterwards the reaction mixture was heated at 120–130 °C for 8 h. About 2/3 of the solvent was removed under reduced pressure at about 80 °C. The reaction mixture was then cooled and diluted with propan-2-ol. The crystalline precipitate of $[\text{Ba}(\text{C}_2\text{H}_6\text{O}_2)_4][\text{Sn}(\text{C}_2\text{H}_4\text{O}_2)_3]$ (**1**) was filtered off, washed with acetone and dried at room temperature. About 1.5 g of precursor **1** was calcined at 1200 °C and the resulting BaSnO_3 powder was dissolved in a 5 M HCl solution at 35 °C. Chemical analyses revealed a Ba/Sn ratio of 1.007.^{34,35} Calcination of **1** at 820 °C in static air led to a very fine BaSnO_3 powder (**1a**).

Additionally, BaSnO_3 powder was also prepared via a conventional mixed-oxide method. BaCO_3 (Sabed VL 600, Solvay) and SnO_2 (Merck) were milled with a molar ratio of 1:1 for 24 h using ZrO_2 -balls in water ($m_{\text{powder}}:m_{\text{balls}}:m_{\text{water}} = 1:1:4$). After filtering off and drying the mixture was calcined in static air

(rate 10 K/min) for 2 h at 1150 °C (**2**), at 1200 °C for 4 h (**3**), and at 1400 °C for 4 h (**4**) respectively. The Ba/Sn ratio of these mixed-oxide powders is 0.999.^{34,35}

For the shrinkage and sintering behaviour the calcined powders (**1a**, **2**, **3**, **4**) were milled with ZrO_2 -balls in propan-2-ol for 2 h ($m_{\text{powder}}:m_{\text{balls}} = 1:4$). After filtering and drying the powders were mixed with 5 mass% of a saturated aqueous solution of polyvinyl alcohol (PVA) as a pressing aid, then the powders were pressed to discs with a green density of about 3.4–3.6 g/cm³.

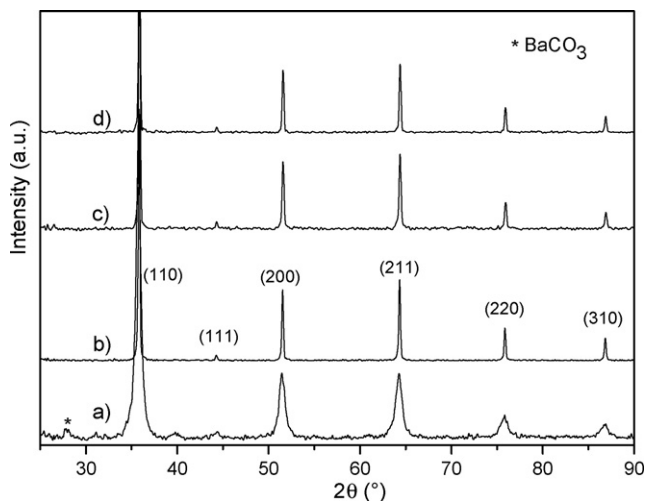


Fig. 2. X-ray powder diffraction patterns (recorded at 25 °C) of powders **1a** (a) and **2** (b), as well as corresponding ceramic bodies of **1a** (c) and **2** (d), sintered at 1500 °C for 1 h (rate: 10 K/min).

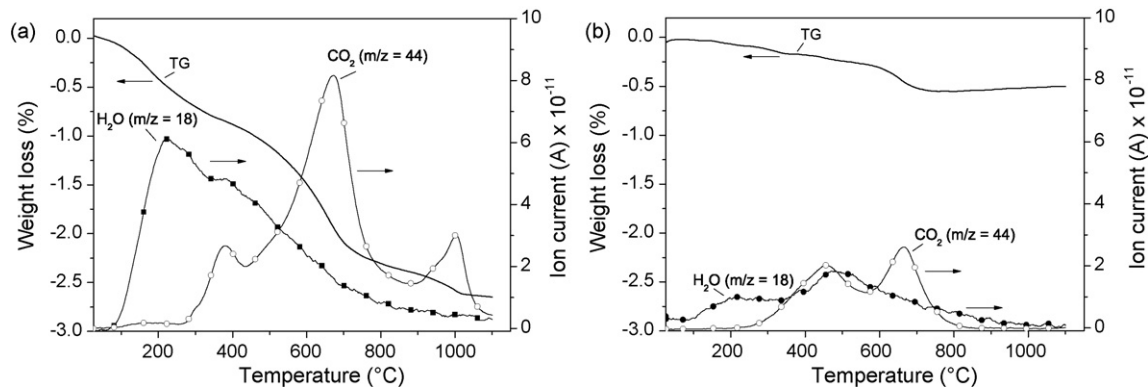


Fig. 3. TG–MS diagrams of powders **1a** (a) and **2** (b). Weighted samples: **1a**, 41.53 mg; **2**, 30.52 mg; heating rate 20 K/min.

2.2. Analytical methods

X-ray powder diffraction (XRD) patterns were recorded by a STADI MP diffractometer from STOE at 25 °C using Co K α ₁ radiation. The powder patterns were indexed and refined with the software suite WinXPOW³⁶ using the TREOR method.³⁷ Fourier transform attenuated total reflection infrared (ATR-IR) spectra in the range 4000–200 cm⁻¹ (resolution: 4 cm⁻¹) were obtained using a Tensor 27 FT-IR spectrometer from Bruker with an ATR unit (MVP 2 Series from Harrick). Simultaneous thermogravimetric and mass spectrometry analysis (TG–MS) were carried out in flowing argon/oxygen (4:1) atmosphere using a STA 409C equipped with a quadrupole mass spectrometer Balzers QMS 421 (Netzsch, Al₂O₃-crucible, heating rate 20 K/min). Dilatometric investigations (shrinkage) were performed in a TMA 92–16.18 unit from Setaram and the densities of the discs were calculated assuming isotropic shrinkage behaviour. The specific surface area was measured using nitrogen three-point BET (Nova 1000, Quantachrome Corporation). The average particle size was calculated assuming the powder particles were spherical or cubic in shape. Crystallite sizes were determined by XRD line broadening using the Scherrer equation³⁸ and the integral peak breadth. Scanning electron microscope images and energy dispersive X-ray analyses (EDX) were recorded by a Philips XL30 ESEM (Environmental Scanning Electron Microscope) and an embedded energy dispersive X-ray spectrometer from Edax.

3. Results and discussion

3.1. Powder characterisation

In our previous work,³² we have reported on a barium tin 1,2-ethanediolato complex precursor – [Ba(HOC₂H₄OH)₄] [Sn(OC₂H₄O)₃] (**1**) – and its decomposition to BaSnO₃ in detail. BaSnO₃ powder with a high specific surface area was obtained by decomposition of **1** by the following thermal treatment: heating to 500 °C with a heating rate of 10 K/min, slow heating with 1 K/min to 820 °C, dwelling time 180 min, followed by cooling at 3 K/min. The resulting white BaSnO₃ powder (**1a**) has a specific surface area of $S = 15.1 \text{ m}^2/\text{g}$ and an average particle size of $d_{\text{av.}} = 55 \text{ nm}$. Crystallite-size measurements by XRD

line broadening³⁸ of the BaSnO₃ reflexions reveal a lower value of about $d_{\text{crys.}} = 26 \text{ nm}$. Discrepancies between the crystallite-/particle size estimated by the XRD line broadening and the specific surface area are reported and explained elsewhere.³⁹ The conventional white mixed-oxide powder **2** has a specific surface area of $4.6 \text{ m}^2/\text{g}$ ($d_{\text{av.}} = 180 \text{ nm}$). SEM images of powder **1a** and **2** are shown in Fig. 1a–d, respectively. Both powders consist of cuboid-like particles.

XRD patterns of powder **1a** and **2** show reflexions of BaSnO₃⁴⁰ (Fig. 2a,b). The diffraction pattern of powder **1a** reveals also traces of BaCO₃.⁴⁰ IR measurements (not shown) also reveal that powder **2** contains small traces of BaCO₃. XRD data (corrected by an internal standard) were indexed on the basis of a primitive cubic unit cell and the cell parameters were determined by least-square refinements. The reported reference lattice parameter for BaSnO₃ from XRD pattern is $a = 411.63 \text{ pm}$.⁴⁰ Single crystal measurements by Megaw revealed a lattice parameter of $a = 411.70 (15) \text{ pm}$ ($\approx 4.1085 \text{ \AA}$),^{41,42} which was also confirmed by Smith and Welch.⁴³ For powder **2** a lattice parameter of $a = 411.69(4) \text{ pm}$ was calculated, whereas a slightly larger lattice constant was found for powder **1a**

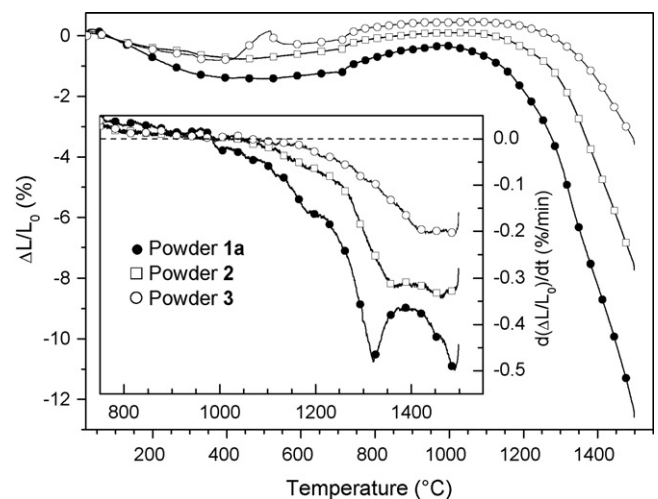


Fig. 4. Shrinkage behaviour (non-isothermal, heating rate 10 K/min) of green bodies of **1a**, **2**, and **3**, respectively. The inset shows the relative shrinkage rate ($d(\Delta L/L_0)/dt$) of these bodies (the green densities are: 3.3 g/cm^3 (**1a**), 3.6 g/cm^3 (**2**), and 3.5 g/cm^3 (**3**)). Every 100th data point is marked by a symbol.

($a = 412.22(7)$ pm). Thermal treatment (analogue procedure as described for **1a**) of precursor **1** at 900°C results in a lattice dimension of $a = 412.02(4)$ pm, at 1000°C of $a = 411.77(5)$ pm, and at 1100°C of $a = 411.63(6)$ pm. Ceramic bodies of **1a** and **2**, sintered at 1500°C for 1 h (Fig. 2c,d), have lattice parameters of $411.64(1)$ pm (**1a**) and $411.67(3)$ pm (**2**), respectively. It can be seen a thermal treatment above 1000°C leads to parameters which do not significantly change with increasing temperature. Buscaglia et al.²³ investigated the decomposition of $\text{BaSn}(\text{OH})_6$ to BaSnO_3 and observed a decreasing cell parameter with increasing annealing temperature, too. By Raman spectroscopy they found that the powders, calcined at very low temperatures, retain a lot of hydroxyl groups inside the lattice, which cause the larger cell parameter. Our IR investigations (ATR-IR) do not reveal a clear evidence for O–H absorption bands. However, TG–MS measurements (Fig. 3) in an argon/oxygen atmosphere of powder **1a** and **2** show the release of CO_2 and H_2O during the thermal treatment to 1100°C in both samples. The powders contain few amounts of BaCO_3 (see above), which cause the release of CO_2 . Single thermogravimetric measurements up to 1100°C in air (not shown) reveal mass losses of about 4.6% (**1a**) and 0.86% (**2**), respectively. The mass losses of the TG–MS measurements (see Fig. 3) are less than of the single thermogravimetric measurements. At the beginning of the TG–MS measurement the equipment (including sample) was flowed through with argon/oxygen gas for 1 h. The mass loss during this time was not recorded.

As can be seen, the release of H_2O takes place in two steps. The first peak at 227°C (**1a**) and 211°C (**2**) is attributed to the evolution of adsorbed water from the surface of the sample, whereas the second peak at about 380°C (**1a**) and 477°C (**2**) is caused by the dehydroxylation of OH groups inside the lattice (protonic defects).^{44,45} The amount of the detected CO_2 and H_2O in powder **2** is lower than in powder **1a**. Therefore, the low amount of OH lattice groups in powder **2** does not significantly influence the lattice constant. We suppose the low amount of protonic defects in powder **2** is created during the cooling phase in a furnace at ambient atmosphere. The amount of lattice OH groups in powder **1a** leads to an increase of the lattice parameter. Even a calcination time of 50 h at 820°C results only in a very slight decrease of the lattice parameter to $412.10(4)$ pm. Protonic defects are investigated for BaTiO_3 and other titanates, very well.^{44,46–49} According to Waser⁴⁹ and Hennings et al.,^{50,51} the lattice OH groups, located on regular oxygen ion sites, cause a positive charge excess compensating by metal vacancies.

3.2. Shrinkage and sintering behaviour

Fig. 4 shows the dilatometric (non-isothermal) investigations to 1500°C (heating rate 10 K/min) of powder compacts of **1a**, **2** and **3**. The theoretical density (single crystal density) of BaSnO_3 ceramics is 7.24 g/cm^3 .⁴⁰

The shrinkage process of powder compacts of **1a** starts at about 980°C . A significant increase of the shrinkage rate is observed at 1130°C and reaches a maximum at about 1183°C . A second pronounced shrinkage process occurs at 1220°C with a rate maximum at 1321°C ($-0.48\%/ \text{min}$). On the verge of the

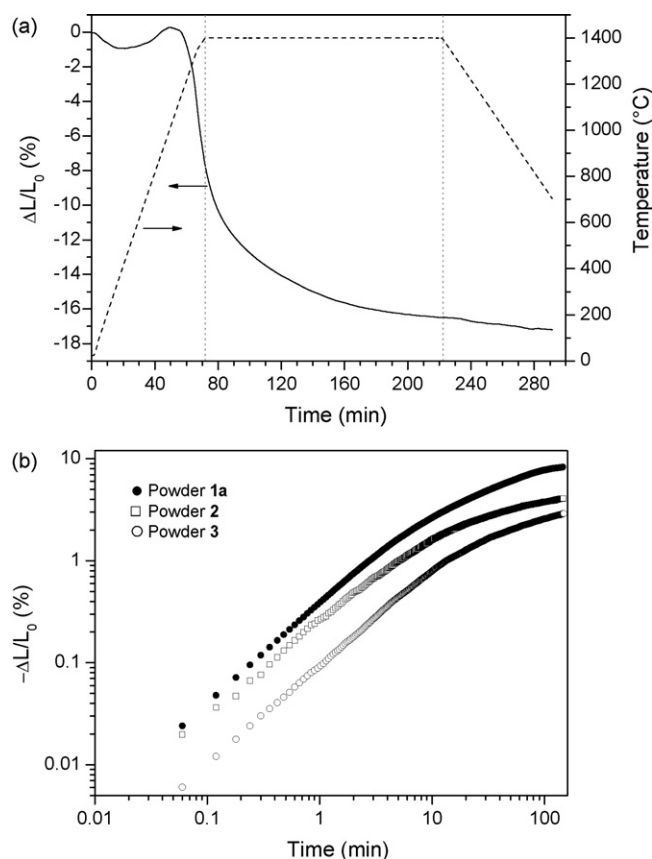


Fig. 5. Isothermal dilatometric investigations of powders **1a**, **2**, **3**, demonstrated at 1400°C ; (a) plot of the whole shrinkage curve (illustrated by the example of powder **1a**); (b) double logarithmic plot of the isothermal segments (the initial values of $\Delta L/L_0$ were set to zero).

end of the heating period a last maximum of the shrinkage rate can be observed at 1489°C (rate: $-0.50\%/ \text{min}$). The sample achieved a relative density of 69% (4.99 g/cm^3) up to the end of the heating process.

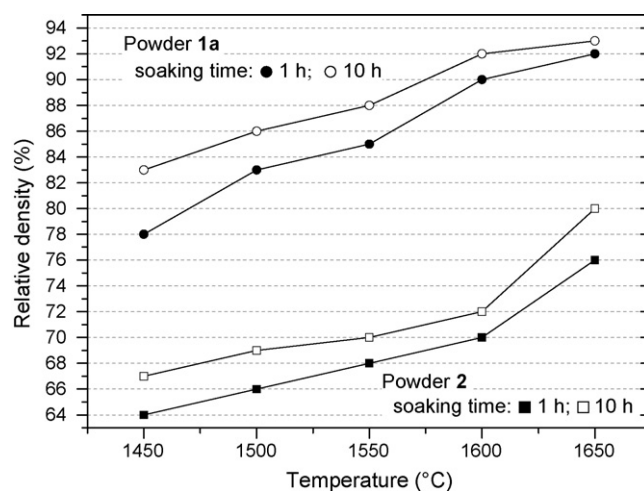


Fig. 6. Final densities of ceramic bodies of **1a** and **2** after an isothermal sintering process at various temperatures at the indicated soaking times in a muffle furnace (heating rate: 10 K/min). The relative densities are related to the theoretical density of 7.24 g/cm^3 .

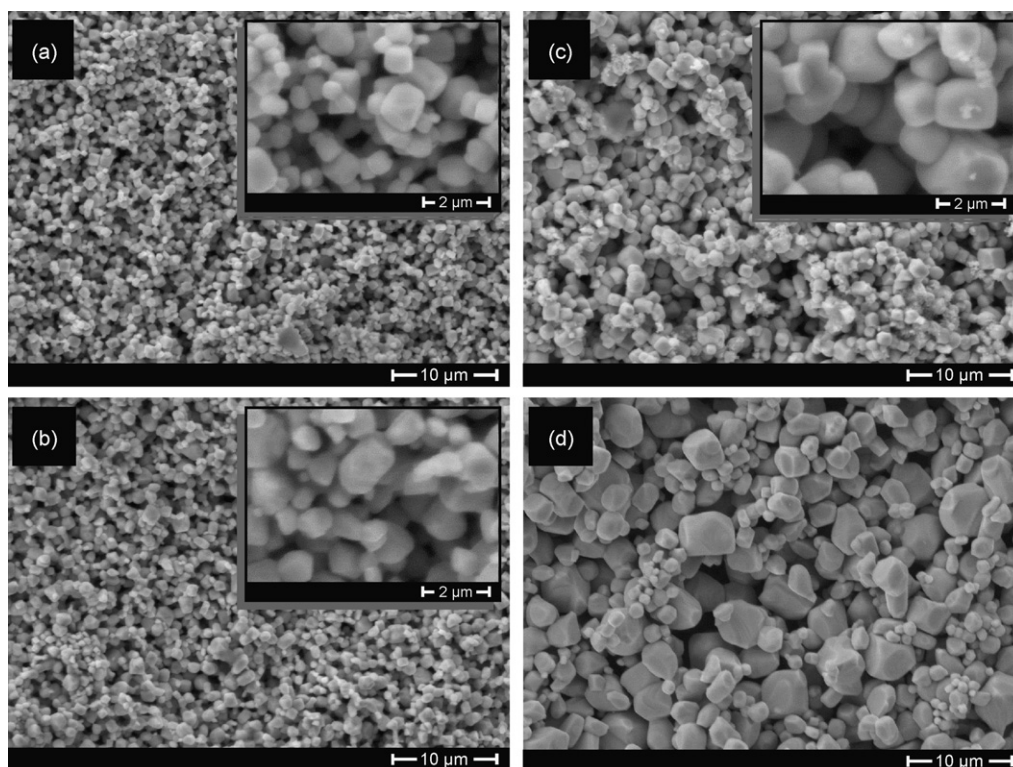


Fig. 7. SEM micrographs of the surfaces of ceramic bodies of **2** after various sintering temperatures and soaking times. (a) 1550 °C, 1 h; (b) 1600 °C, 1 h; (c) 1650 °C, 1 h; (d) 1600 °C, 10 h.

Sample **2** slowly starts to shrink at 1055 °C, however a significant shrinkage process appears at about 1190 °C and shows two maxima of the shrinkage rate at 1365 °C and 1462 °C. The shrinkage rates at these maxima are -0.32 and $-0.34\%/min$. The shrinkage curve of **2** reveals an increasing densification to the end of the heating period and reaches 64% (4.65 g/cm^3) of the theoretical density. Powder (**3**) ($S = 2.6 \text{ m}^2/\text{g}$; $d_{\text{ava.}} = 319 \text{ nm}$) shows analogous shrinkage behaviour, however the whole shrinkage is lower. The maxima of the shrinkage rate appear at about 1430 °C ($-0.20\%/min$) and 1489 °C ($-0.21\%/min$). Up to 1500 °C the relative density reaches a value of 54% (3.90 g/cm^3).

The observed shrinkage rates at the maxima of **1a**, **2** and **3** ($d(\Delta L/L_0)/dt = -0.20 - -0.50\%/min$) cannot be explained by diffusion processes alone. Diffusion as the dominant process causes shrinkage rates of about $10^{-4} - 10^{-1}\%/min$.⁵² Therefore, the observed shrinkage rates hint that the shrinkage is also caused by sliding processes of whole grains (also described as superplastic deformation^{52,53}).

Isothermal dilatometric investigations allow to determine the dominant shrinkage mechanism, depending on the sintering time. The samples for these investigations were heated with a rate of 20 K/min. The heating rate was lowered to 10 K/min 50 K below the isothermal plateau was reached. The investigations for compacts of **1a** were carried out at several isothermal plateaus between 1150–1550 °C. The temperature ranges for powder **2** and **3** were set between 1220–1550 °C and 1400–1550 °C, respectively, because we did not observe a sufficient shrinkage below these ranges. The general approach of the isothermal investigations is reported elsewhere.^{39,54} A representation of the

logarithm of $\Delta L/L_0$ versus the logarithm of time (t) of the isothermal part (150 min) allows to verify the dominating shrinkage mechanism.^{54,55} Fig. 5 exemplarily shows the isothermal curves for compacts of powder **1a**, **2** and **3** at 1400 °C. The isothermal shrinkage process is divided into two sections (different slopes) representing different shrinkage mechanisms⁵⁵ (see following equation).

$$\left(\frac{\Delta L}{L_0}\right)^{m/2} = -\frac{H}{2^m R^n} t \quad (1)$$

Here, $\Delta L/L_0$ is the relative shrinkage, H is a function containing material parameters, R is the radius of the particles, t is the time, n and m are numerical exponents depending on the shrinkage mechanism ($m = 2 \rightarrow$ viscous flow; $m = 5 \rightarrow$ lattice diffusion from the grain boundary; $m = 6 \rightarrow$ grain boundary diffusion).

The first segment of the isothermal curves has a slope according to a shrinkage exponent of $m = 2$ indicating viscous flow as the major shrinkage mechanisms. The slope of the second segment is of the order of 0.32–0.5 and m is calculated to 4–6. Consequently, the shrinkage in the second stage is dominated by grain boundary diffusion and volume diffusion from the grain boundaries. It can be seen that the beginning of the shrinkage process is always dominated by viscous flow process, similar to the shrinkage behaviour of BaTiO₃-based ceramics.^{39,54,56} Even a very coarse-grained mixed-oxide powder (**4**) ($S = 1.02 \text{ m}^2/\text{g}$, $d_{\text{av.}} = 812 \text{ nm}$), investigated at 1550 °C, revealed also sliding processes in the first stage of shrinkage. A necessary presupposition for such sliding processes of whole grains is the existence of

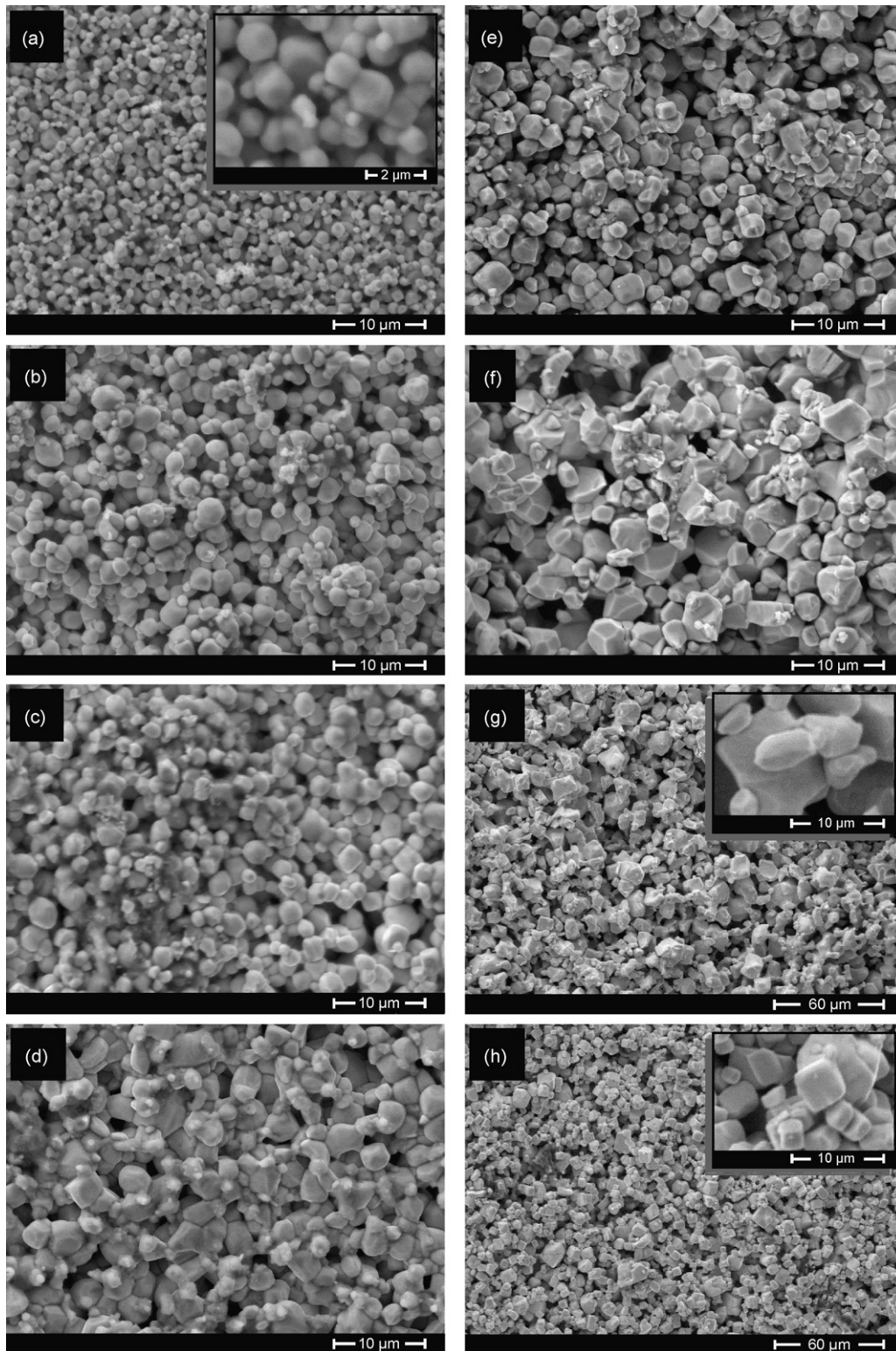


Fig. 8. SEM micrographs of the surfaces of ceramic bodies of **1a** after various sintering temperatures and soaking times. (a) 1450 °C, 1 h; (b) 1550 °C, 1 h; (c) 1600 °C, 1 h; (d) 1650 °C, 1 h; (e) 1550 °C, 10 h; (f) 1600 °C, 10 h; (g) 1650 °C, 10 h; (h) 1500 °C, 30 h.

amorphous or defect-rich contact boundaries.^{52,57–59} By means of the higher shrinkage rates and the better densification, sliding processes in compacts of **1a** are more dominant than in compacts of **2** and **3**. Powders with small particle sizes have a large

amount of (defect-rich) grain boundaries, which are responsible for the appearance of sliding processes.⁵⁷ Dror et al.⁵⁶ described the grain boundaries as amorphous areas surrounding crystalline cores, which promote the sliding processes.

The above-mentioned classification of the appearing mechanisms (first → viscous flow, second → diffusion processes) is found for all investigated BaSnO₃ powders and temperatures.

Fig. 6 shows the final bulk densities of ceramic bodies of **1a** and **2** (calculated from their weight and geometric dimensions) depending on the sintering temperature and soaking time. In agreement with the results of other authors,^{17,60} green bodies of **2** show an insufficient shrinkage behaviour. Even at 1650 °C and a soaking time of 10 h we do not obtain dense ceramic bodies of ≥90% of the relative density. SEM images of these bodies reveal a porous microstructure and show typical cubic-like grains⁶¹ (Fig. 7a–c). However, from a temperature of 1600 °C and 10 h sintering, we observe a gradual change to globular-like or irregular grains (Fig. 7d). After sintering at 1450 °C and a soaking time of 1 h the ceramic bodies consist of grains between about 0.5–1.1 μm, which grow to 0.8–2.4 μm at 1650 °C. A prolonged soaking time of 10 h only leads to a grain growth to 1.3–7 μm at 1650 °C. In contrast, ceramic bodies of **1a** show a considerable better densification behaviour. Even at 1450 °C the ceramics have relative densities of 78% (5.64 g/cm³) and 83% (6.01 g/cm³) after sintering of 1 and 10 h, respectively. A soaking time of 1 h and a sintering temperature of 1600 °C lead to ceramic bodies with a density of 90% (6.50 g/cm³) and a soaking time of 10 h raises the density to 92% (6.69 g/cm³). At a sintering temperature of 1650 °C we observe a slight increase of the densities to 6.67 g/cm³ (92%) and 6.75 g/cm³ (93%) after 1 and 10 h, respectively. Sintering for 1 h leads to grain sizes of 0.65–2 μm (1450 °C), 0.9–2.8 μm (1550 °C), and 1.6–4 μm (1650 °C). After sintering of 10 h the grains grow from 0.9–2.6 μm (1450 °C) to 3–21 μm (1650 °C). Dense ceramic bodies, with grain sizes of 3–13 μm, can be also obtained after sintering at 1500 °C for 30 h (6.53 g/cm³, 90% rel. density). SEM images (Fig. 8) of ceramics of **1a** show, that these ceramics consist of cubic-like grains up to about 1550 °C, however higher temperatures and soaking times gradually lead to an irregular shape of the grains (see Fig. 8f,g).

In particular at sintering temperatures of 1600 and 1650 °C and longer soaking times, we observe a considerable mass loss of our ceramic bodies. Sintering at 1650 °C of green bodies of **2** (disc, $\varnothing \approx 6$ mm, shortly preheated to 1650 °C to remove the PVA binder and possible traces of carbonates) for 10 h show a mass loss of about 16%, which increases with raising sintering time (20 h) to 34%. Samples of powder **1a** exhibit comparable mass losses. XRD patterns after these investigations reveal the samples consist of BaSnO₃ as the only crystalline phase. No second phases, e.g. Ba₂SnO₄, could be detected. EDX analyses of ceramics (**2**) sintered at 1550 °C for 1 h, 1650 °C for 1 h and 20 h did not show any significant change in the Ba/Sn ratio. Therefore the mass loss primarily results from the evaporation of BaSnO₃ and is not caused by the evaporation of SnO₂ (decomposition) as observed at temperatures above 1800 °C.¹⁷

4. Conclusion

The shrinkage behaviour and mechanism of fine and coarse-grained BaSnO₃ powder, prepared via a precursor and a mixed-oxide method were investigated. Calcination of a

[Ba(HOC₂H₄OH)₄][Sn(OC₂H₄O)₃] (**1**) precursor at 820 °C leads to a very fine BaSnO₃ powder (**1a**) with a specific surface area of 15.1 m²/g ($d_{av.} = 55$ nm) and a slightly larger cell parameter of $a = 412.22(7)$ pm in comparison to the reference parameter. Coarse-grained samples (**2**), prepared by the mixed-oxide method ($S = 4.6$ m²/g, $d_{av.} = 180$ nm), show an insufficient sintering behaviour. Up to 1650 °C and a soaking of 10 h the compacts reaches a relative bulk density of 80%. The porous ceramics consist of cubic grains. In contrast the fine-grained (nm-sized) powder **1a** reveal a considerable improvement of the sintering behaviour. Ceramics with at least 90% of the single crystal density can be obtained at 1600 or at 1500 °C and very long soaking time. Ceramic bodies with cubic grains are observed up to a sintering temperature of 1550 °C, higher temperatures leads to an irregular shape.

Isothermal dilatometric investigations show that the shrinkage of the investigated fine and coarse-grained powder compacts is characterized by sliding and diffusion processes. In particular, the beginning of the shrinkage process is always dominated by viscous flow, independent from the particle sizes of the powders. On the basis of the maxima of the shrinkage rates (non-isothermal), it can be seen the influence of the sliding processes decreases with increasing grain sizes of the powders.

Acknowledgements

The authors would like to thank Dr. Th. Müller for dilatometric and XRD measurements, F. Syrowatka for EDX measurements and Dr. J. Hanss (University of Augsburg) for TG–MS investigations. We are also grateful to Dr. D. Völtzke (Rauschert Hermsdorf GmbH) for his helpful discussions. Financial support by the Federal State Saxony-Anhalt (Cluster of Excellence “Nanostructured Materials”) is gratefully acknowledged.

References

1. Vivekanandan, R. and Kutty, T. R. N., Grain boundary layer ceramic capacitors based on donor-doped Ba(Ti_{1-x}Sn_x)O₃. *Mater. Sci. Eng. B*, 1990, **6**(4), 221–231.
2. Zhou, Z. G., Zhao, G., Wei, M. and Zhang, Z. T., Temperature–humidity–gas multifunctional sensitive ceramics. *Sens. Actuators*, 1989, **19**, 71–81.
3. Singh, P., Brandenburg, B. J., Sebastian, C. P., Singh, P., Singh, S., Kumar, D. and Parkash, O., Electronic structure, electrical and dielectric properties of BaSnO₃ below 300 K. *Jpn. J. Appl. Phys.*, 2008, **47**, 3540–3545.
4. Movchikova, A., Malyskina, O., Suchanek, G., Gerlach, G., Steinhausen, R., Langhammer, H. T., Pientischke, C. and Beige, H., Study of the pyroelectric behavior of BaTi_{1-x}Sn_xO₃ piezo-ceramics. *J. Electroceram.*, 2008, **20**, 43–46.
5. Wang, T., Chen, X. M. and Zheng, X. H., Dielectric characteristics and tunability of barium stannate titanate ceramics. *J. Electroceram.*, 2003, **11**, 173–178.
6. Ostrick, B., Fleischer, M., Hampe, U. and Meixner, H., Preparation of stoichiometric barium stannate thin films: Hall measurements and gas sensitivities. *Sens. Actuators B*, 1997, **44**, 601–606.
7. Tao, S., Gao, F., Liu, X. and Sørensen, O. T., Ethanol-sensing characteristics of barium stannate prepared by chemical precipitation. *Sens. Actuators B*, 2000, **71**, 223–227.
8. Lampe, U., Gerblinger, J. and Meixner, H., Carbon-monoxide sensors based on thin films of BaSnO₃. *Sens. Actuators B*, 1995, **24–25**, 657–660.

9. Hodjati, S., Vaezzadeh, K., Petit, C., Pitchon, V. and Kiennemann, A., NO_x sorption–desorption study: application to diesel and lean-burn exhaust gas (selective NO_x recirculation technique). *Catal. Today*, 2000, **59**, 323–334.
10. McGeehin, P. and Williams, D. E. Sensing gaseous substances. International Application, Patent No. WO 9308467 A1 19930429, 1993.
11. Gopal Reddy, C. V., Manorama, S. V. and Rao, V. J., Preparation and characterization of barium stannate: application as a liquefied petroleum gas sensor. *J. Mater. Sci.: Mater. Electron.*, 2001, **12**, 137–142.
12. Chu, X., Dilute CH₃SH-sensing characteristics of BaSnO₃ thick film sensor. *Mater. Sci. Eng. B*, 2004, **106**, 305–307.
13. Borse, P. H., Lee, J. S. and Kim, H. G., Theoretical band energetics of Ba(M_{0.5}Sn_{0.5})O₃ for solar photoactive applications. *J. Appl. Phys.*, 2006, **100**, 124915–124921.
14. Borse, P. H., Joshi, U. A., Ji, S. M., Jang, J. S., Lee, J. S., Jeong, E. D. and Kim, H. G., Band gap tuning of lead-substituted BaSnO₃ for visible light photocatalysis. *Appl. Phys. Lett.*, 2007, **90**, 034103–034111.
15. Yuan, Y., Lv, J., Jiang, X., Li, Z., Yu, T., Zou, Z. and Ye, J., Large impact of strontium substitution on photocatalytic water splitting activity of BaSnO₃. *Appl. Phys. Lett.*, 2007, **91**, 094107–094111.
16. Mizoguchi, H., Woodward, P. M., Park, C. and Keszler, D. A., Strong near-infrared luminescence in BaSnO₃. *J. Am. Chem. Soc.*, 2004, **126**, 9796–9800.
17. Wagner, G. and Binder, H., Untersuchung der binären Systeme BaO–SnO₂ und BaO–PbO₂. I. Phasenanalysen. *Z. Allg. Anorg. Chem.*, 1958, **297**, 328–346.
18. Upadhyay, S., Parkash, O. and Kumar, D., Solubility of lanthanum, nickel and chromium in barium stannate. *Mater. Lett.*, 2001, **49**, 251–255.
19. Kutty, T. R. N. and Vivekanadan, R., BaSnO₃ fine powders from hydrothermal preparations. *Mater. Res. Bull.*, 1987, **22**, 1457–1465.
20. Cerda, J., Arbiol, J., Diaz, R., Dezanneau, G. and Morante, J. R., Synthesis of perovskite-type BaSnO₃ particles obtained by a new simple wet chemical route based on a sol–gel process. *Mater. Lett.*, 2002, **56**, 131–136.
21. Udawatte, C. P. and Yoshimura, M., Preparation of well-crystallized BaSnO₃ powders under hydrothermal conditions. *Mater. Lett.*, 2001, **47**, 7–10.
22. Leoni, M., Viviani, M., Nanni, P. and Buscaglia, V., Low-temperature aqueous synthesis (LTAS) of ceramic powders with perovskite structure. *J. Mater. Sci. Lett.*, 1996, **15**, 1302–1304.
23. Buscaglia, M. T., Leoni, M., Viviani, M., Buscaglia, V., Martinelli, A., Testino, A. and Nanni, P., Synthesis and characterization of BaSn(OH)₆ and BaSnO₃ acicular particles. *J. Mater. Res.*, 2003, **18**(3), 560–566.
24. Pfaff, G., Wet chemical powders synthesis of BaSnO₃ and Ba₂SnO₄. *J. Eur. Ceram. Soc.*, 1993, **12**, 159–164.
25. Lu, W. and Schmidt, H., Lyothermal synthesis of nanocrystalline BaSnO₃ powders. *Ceram. Inter.*, 2008, **34**, 645–649.
26. Udawatte, C. P., Kakihana, M. and Yoshimura, M., Preparation of pure perovskite-type BaSnO₃ powders by the polymerized complex method at reduced temperature. *Solid State Ionics*, 1998, **108**, 23–30.
27. Lu, W. and Schmidt, H., Synthesis of nanosized BaSnO₃ powders from metal isopropoxides. *J. Sol-Gel Sci. Technol.*, 2007, **42**, 55–64.
28. Song, Y. J. and Kim, S., Preparation of BaSnO₃ powders by oxalate coprecipitation method. *J. Ind. Eng. Chem.*, 2001, **7**(3), 183–185.
29. Jäger, L., Lorenz, V., Müller, T., Abicht, H.-P., Rössel, M. and Görls, H., Barium stannate powders from hydrothermal synthesis and by thermolysis of barium-tin(IV)-glycolates. Synthesis and structure of [Ba(C₂H₆O₂)₄] [Sn(C₂H₄O₂)₃] and [Ba(C₂H₆O₂)₂][Sn(C₂H₄O₂)₃].CH₃OH. *Z. Anorg. Allg. Chem.*, 2004, **630**, 189–195.
30. Aguas, M. D., Morris, L. and Parkin, I. P., Self-propagating solid state routes to BaSnO₃: investigation of gas sensing properties. *J. Mater. Sci.*, 2002, **37**, 375–379.
31. Azad, A.-M., Shyan, L. L. W., Pang, T. Y. and Nee, C. H., Microstructural evolution in MSnO₃ ceramics derived via self-heat-sustained (SHS) reaction technique. *Ceram. Inter.*, 2000, **26**, 685–692.
32. Köferstein, R., Abicht, H.-P., Woltersdorf, J. and Pippel, E., Phase evolution of a barium tin 1,2-ethanediolate complex to barium stannate during thermal decomposition. *Thermochim. Acta*, 2006, **441**, 176–183.
33. Köferstein, R., Jäger, L., Lorenz, V., Abicht, H.-P., Woltersdorf, J., Pippel, E. and Görls, H., Mixed crystalline precursor complexes of the type [Ba(C₂H₆O₂)₄][Ti_{1-x}Sn_x(C₂H₄O₂)₃] (x = 0–1) for BaTi_{1-x}Sn_xO₃ ceramics: Synthesis, structure and calcination. *Solid State Sci.*, 2005, **7**, 1280–1288.
34. Price, J. W. and Smith, R., *Handbook of Analytical Chemistry, part III, vol. 4a*. Springer-Verlag, Berlin, Heidelberg, New York, 1978, p. 9.
35. Kodama, K., *Methods of Quantitative Inorganic Analysis*. Interscience Publishers, New York, 1963, p. 205.
36. Program WinXPOW v1.06, Stoe & Cie GmbH, Darmstadt, 1999.
37. Werner, P.-E., Eriksson, L. and Westdahl, M., TREOR, a semi-exhaustive trial-and-error powder indexing program for all symmetries. *J. Appl. Cryst.*, 1985, **18**, 367–370.
38. Birks, L. S. and Friedman, H., Particle size determination from X-ray line broadening. *J. Appl. Phys.*, 1946, **17**, 687–692.
39. Köferstein, R., Jäger, L., Zenkner, M., Müller, T. and Abicht, H.-P., Shrinkage mechanism and phase evolution of fine-grain BaTiO₃ powder compacts containing 10 mol% BaGeO₃ prepared via a precursor route. *Mater. Chem. Phys.*, 2008, **112**, 531–535.
40. PDF 2 (International Centre for Diffraction Data, Pennsylvania), BaSnO₃ [15–780_{cubic}], BaCO₃ [5–378_{orthorhombic}], 2001.
41. Megraw, H. D., Crystal structure of double oxides of the perovskite type. *Proc. Phys. Soc. Lond.*, 1946, **58**, 133–152.
42. Bearden, J. A., X-ray wavelengths. *Rev. Mod. Phys.*, 1967, **39**(1), 78–124.
43. Smith, A. J. and Welch, A. J. E., Some mixed metal oxides of perovskite structure. *Acta Cryst.*, 1960, **13**, 653–656.
44. Jena, H., Kutty, K. V. G. and Kutty, T. R. N., Proton transport and structural relations in hydroxyl-bearing BaTiO₃ and its doped compositions synthesised by wet-chemical methods. *Mater. Res. Bull.*, 2004, **39**, 489–511.
45. Atakam, V., Chen, C. W., Paul, R. and Riman, R. E., Quantification of hydroxyl content in ceramic oxides: A prompt γ activation analysis study of BaTiO₃. *Anal. Chem.*, 2008, **80**, 6626–6632.
46. Stashansy, A. and Chimborazo, J., Effect of interstitial hydrogen on structural and electronic properties of BaTiO₃. *Phil. Mag. B*, 2002, **82**(10), 1145–1154.
47. Busca, G., Buscaglia, V., Leoni, M. and Nanni, P., Solid-state and surface spectroscopic characterization of BaTiO₃ fine powders. *Chem. Mater.*, 1994, **6**, 955–961.
48. Kreuer, K. D., Aspects of the formation and mobility of protonic charge carriers and the stability of perovskite-type oxides. *Solid State Ionics*, 1999, **125**, 285–302.
49. Waser, R., Solubility of hydrogen defects in doped and undoped BaTiO₃. *J. Am. Ceram. Soc.*, 1988, **71**(1), 58–63.
50. Hennings, D. F. K., Metzmaier, C. and Schreinemacher, B. S., Defect chemistry and microstructure of hydrothermal barium titanate. *J. Am. Ceram. Soc.*, 2001, **84**(1), 179–182.
51. Hennings, D. and Schreinemacher, S., Characterisation of hydrothermal barium titanate. *J. Eur. Ceram. Soc.*, 1992, **9**, 41–46.
52. Schatt, W., *Sintervorgänge*. VDI-Verlag, Düsseldorf, 1992, pp. 78–100.
53. Novikov, I. I. and Portnoj, V. K., *Superplastizität von Legierungen*. Deutscher Verlag für Grundstoffindustrie, Leipzig, 1984, p. 12 et seqq.
54. Völtzke, D. and Abicht, H.-P., The influence of different additives and the mode of their addition on the sintering behavior and the properties of semiconducting barium titanate ceramics. *Solid State Sci.*, 2000, **2**, 149–159.
55. Rahaman, M. N., *Ceramic Processing and Sintering*. Marcel Dekker, New York, 1995, p. 398 et seqq.
56. Dror, Y., Levi, R. D., Baltianski, S. and Tsour, Y., Identification of the early stage of sintering of nano-BaTiO₃. A comparative study. *J. Electrochem. Soc.*, 2006, **153**(7), F137–F143.
57. Schatt, W., Vorgänge beim Festphasensintern und ihre Verallgemeinerungsfähigkeit. *Z. Metallkde.*, 1989, **80**(11), 809–816.
58. Geguzin, Ya. E. and Klinchuk, Yu. I., Mechanism and kinetics of the initial stage of the solid-phase sintering of pressed parts from crystal-body powders activity during sintering. *Poroshkovaya Metallurgiya*, 1976, **7**, 17–25.
59. Schatt, W., Study of sintering processes by positron annihilation. *Solid State Phenomena*, 1992, **25–26**, 23–28.
60. Upadhyay, S., Parkash, O. and Kumar, D., Preparation and characterisation of barium stannate BaSnO₃. *J. Mater. Sci. Lett.*, 1997, **16**, 1330–1332.
61. Azad, A.-M., Hashim, M., Baptist, S., Badri, A. and Haq, A. U. L., Phase evolution and microstructural development in sol–gel derived MSnO₃ (M = Ca, Sr and Ba). *J. Mater. Sci.*, 2000, **35**, 5475–5483.